Accepted Manuscript

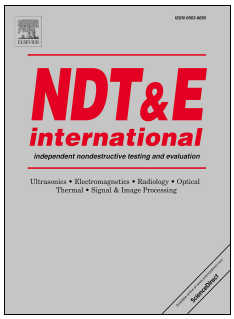

Detection and reconstruction of complex structural cracking patterns with electrical imaging

Danny Smyl, Mohammad Pour-Ghaz, Aku Seppänen

PII: S0963-8695(18)30235-4

DOI: 10.1016/j.ndteint.2018.06.004

Reference: JNDT 2000

To appear in: *NDT and E International*

Received Date: 13 April 2018

Revised Date: 15 June 2018

Accepted Date: 27 June 2018

Please cite this article as: Smyl D, Pour-Ghaz M, Seppänen A, Detection and reconstruction of complex structural cracking patterns with electrical imaging, *NDT and E International* (2018), doi: 10.1016/j.ndteint.2018.06.004.

Detection and reconstruction of complex structural cracking patterns with electrical imaging

Danny Smyl[a,*], Mohammad Pour-Ghaz[b], Aku Seppänen[c]

[a]*Department of Mechanical Engineering, Aalto University, Espoo, Finland*
[b]*Department of Civil, Construction, and Environmental Engineering, North Carolina State University, Raleigh, NC*
[c]*Department of Applied Physics, University of Eastern Finland, Kuopio, Finland*

Abstract

The ability to detect cracks in structural elements is an integral component in the assessment of structural heath and integrity. Recently, Electrical Resistance Tomography (ERT) -based *sensing skins* have been shown to reliably image progressive surface damage on structural members. However, so far the approach has only been tested in cases of relatively simple crack patterns. Because the spatial resolution of ERT is generally low, it is an open question whether the ERT-based sensing skins are able to image complex structural cracking patterns. In this paper, we test the accuracy of ERT for reconstructing cracking patterns experimentally and computationally. In the computational study, we use a set of numerical simulations that model progressive cracking in a rectangular beam geometry. We also investigate the effect of image reconstruction methods on the crack pattern estimates: In addition to the contemporary image reconstruction method used in the recent sensing skin studies, we test the feasibility of a novel approach where model-based structural prior information on the cracking probability is accounted for in the image reconstruction. The results of this study indicate that ERT-based sensing skins are able to detect and reconstruct complex structural cracking patterns, especially when structural prior information is utilized in the image reconstruction.

Keywords: Damage Detection, Finite Element Analysis, Image Analysis, Inverse Problem

1. Introduction

The detection of damage in structures is paramount in the assessment of safety, functionality, and serviceability of structures. In practice, numerous processes may contribute to progressive structural damage. Broadly speaking, these contributors may include cracking of reinforced concrete, corrosion of metallic structural members, localized damage due to impact, fatigue, fracture, excessive plastic deformation, and much more [1, 2, 3, 4].

Some popular methods used for detecting local and/or distributed damage utilize optical [5], image-correlating [6], ultrasonic [7, 8], capacitive [9, 10], or direct-strain [11] modalities. Recently, the use of electrically-conductive sensing skins coupled with Electrical Resistance Tomography (ERT) for imaging spatially-distributed damage has been a source of much research interest [12, 13, 14, 15, 16, 17]. In related works, the use of ERT to monitor moisture flow in cement-based materials, a significant contributer to environmental degradation, in two- and three-dimensions was shown in [18, 19, 20, 21]. In [22], the ERT-based sensing skin was shown to be feasible for detecting corrosive agents on the concrete surface. In [23], ERT was used to detect carbonation in cement-based materials.

In ERT, surface measurements are taken and images of the electrical conductivity distribution are reconstructed by numerically solving the ERT inverse problem. The attractiveness of ERT is often centered around the low monetary cost, minimal space requirements, and rapidity of measurements. Some disadvantages of ERT are the sensitivity to measurement noise and modeling errors [24, 25] and the high-computational cost when using fine meshes with iterative minimization regimes [26, 27]. On the other hand, the computational

*Corresponding author
Email address: danny.smyl@aalto.fi (Danny Smyl)

cost of ERT could be reduced by implementing some of the available direct, non-iterative reconstruction methods, such as D-bar [28, 29], factorization [30, 31] or monotonicity [32, 33, 34] methods, or by applying model reduction methods in the Bayesian framework [35, 36].

Processes visualized by ERT, such as flow of moisture and corrosive agents, and carbonation are generally processes with spatial smoothness and are therefore well-suited for detection using ERT [24]. On the other hand, the detection of sharp changes in conductivity resulting from mechanically-induced crack development has caused significant challenges in ERT imaging [37]. In [38] and [22] these challenges were addressed by approximating the model error and using Total Variation (TV) regularization to capture sharp conductivity distributions. The ERT images of cracking presented in these works captured the location and geometry of simple cracking patterns with up to three cracks.

The feasibility of the ERT to detect dense and complicated cracking patterns is currently unknown. Since cracking patterns in built structures often contain numerous cracks which may occur in dense configurations, this problem is of practical interest. While cracking geometry in such configurations may be complex, much information regarding the probable location of cracks is available through structural modeling [39]. Coupled with information related to the state and distribution of electrical properties in sensing skins, *a priori* information may be useful in imaging complex structural cracking patterns.

As alluded to in this section, a central theme in this article is the use of electrical imaging based sensing skins for damage monitoring. In particular, we study whether the ERT based sensing skin may be used for detecting and reconstructing complex structural cracking patterns on surfaces of solid structures. The sensing skin consists an electrically-conductive area sensor affixed to the surface of a structure. The sensor may be constructed from a broad suite of materials; most commonly, carbon-based sheets [13] or metallic-based paints [22, 15]. When coupled with ERT measurements (current injections I and electric potential measurements $V_1, V_2, ...$), the changes on the structure surface (such as cracking, strain or presence of corroding agents) can be localized by reconstructing the electrical conductivity distribution of the sensing skin. To illustrate the case of imaging surface breaking cracks, Fig. 1 shows photographs/schematics of a sensing skin setup, and corresponding images provided by the sensing skin in an ideal case. Fig. 1 also highlights the target technical problem of this article: imaging of complex crack patterns.

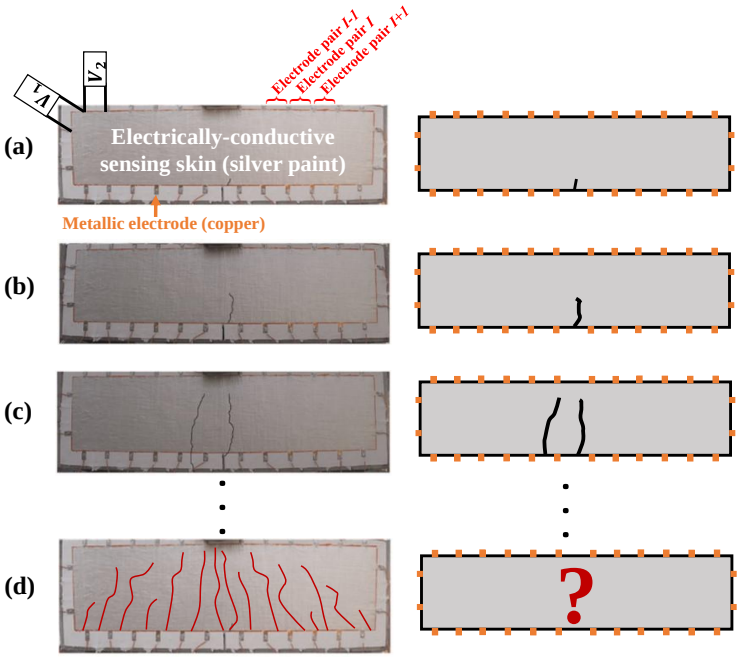

Figure 1: Photographs/schematics representing an ERT based sensing skin setup (left column) and illustrative crack reconstructions (right column) in cases of four qualitative levels of crack pattern complexity: (a) low (b) low-medium, (c) medium and (d) high complexity. The far right hand side image with a "?" indicates the target technical problem of the article: whether electrical imaging may be used for detecting and reconstructing complex cracking patterns, such as those highlighted in maroon.

In addition to the primary aim of the article, we study the effect of background conductivity of the sensing skin on the ERT-based cracking pattern estimates. We compare the performance of two computational approaches to ERT image reconstruction. The first image reconstruction method is equivalent to the approach used in the recent studies [38, 22] and is denoted the "contemporary" reconstruction approach. In the contemporary approach, a simple model-error correction method is used to acf for the uncertainty of the background conductivity of the sensing skin, i.e. the conductivity before cracking. The second approach to ERT image reconstruction is adopted from [40, 41] and is denoted the "non-linear difference imaging" reconstruction approach. In the non-linear difference imaging approach, pre-cracked and post-cracked states of the sensing skin conductivity are reconstructed simultaneously based on ERT measurements corresponding to both states. Moreover, the latter image reconstruction scheme is further elaborated, by constraining the crack patterns to a region of interest which is extracted from structural modeling. The feasibility of the ERT reconstructions is first demonstrated by experimental data from a mechanically-loaded concrete beam. Next, the capability of ERT-based sensing skin to image complex crack patterns on a set of different background conductivities is tested by numerical simulations. Concisely, the aims of this work are:

- Determine whether electrical imaging may be used for detecting and reconstructing complex structural cracking patterns that occur in sensing skins.
- Propose a framework for incorporating prior information from structural modeling into ERT.
- Test the contemporary and non-linear difference imaging approaches, using experimental and numerical data, to determine their feasibility at reconstructing progressively complex cracking patterns.
- Study the effect of background inhomogeneity on reconstruction quality.

2. ERT imaging scheme

2.1. Overview

The purpose of ERT is to reconstruct the internal distribution of electrical conductivity using electric potential measurements from the surface of the object/structure. There are numerous practical applications of ERT, for example, in medical imaging [42], geophysics [43, 44], and structural damage detection [13]. The ERT reconstruction schemes are commonly divided into two categories: *difference* and *absolute* imaging. In difference imaging, a *change* of a temporally varying conductivity distribution is reconstructed based on measured potentials corresponding to states before and after the change. In absolute imagining, reconstructions are computed based on measurements corresponding to a single state.

In recent works [21, 22], the ERT reconstructions were also computed by utilizing reference data from an intact sensing skin (prior to cracking) when reconstructing the conductivity distribution of the cracked sensing skin. However, unlike in conventional, linearized difference imaging, the reference data was used for constructing an approximate modeling error term which was included in the observation model, and the reconstructions corresponding to cracked state were computed by solving a non-linear inverse problem. This approach – which was shown to capture the crack patterns better than linearized difference imaging [21] – is reviewed below in Section 2.3.1. As an alternative reconstruction method, we consider the non-linear difference imaging scheme proposed in [40, 41], see Section 2.3.2.

2.2. Forward model

In this work, the dependence between the electrical conductivity distribution σ and electrode potentials U is described by the so-called Complete Electrode Model (CEM) which consists of the partial differential equation

$$\nabla \cdot (\sigma \nabla u) = 0, \quad x \in \Omega \tag{1}$$

and the boundary conditions

$$u + \xi_l \sigma \frac{du}{d\bar{n}} = U_l, \quad x \in e_\ell, \ \ell = 1, \ldots, L \tag{2}$$

$$\sigma \frac{du}{d\bar{n}} = 0, \quad x \in \partial\Omega \backslash \bigcup_{\ell=1}^{L} e_\ell \tag{3}$$

$$\int_{e_l} \sigma \frac{du}{d\bar{n}} \, dS \; = I_l, \quad \ell = 1, \ldots, L \tag{4}$$

where Ω is the target domain, $\partial\Omega$ is its boundary, u is the electric potential, $\bar{n}$ is the outward unit normal, and e_l is the l^{th} electrode [45, 46]. Further, ξ_l, U_l and I_l, respectively, are the contact impedance, electric potential, and electrical current corresponding to e_l. Moreover, the current conservation law must be fulfilled

$$\sum_{l=1}^{L} I_l = 0 \tag{5}$$

and the potential reference level must be fixed, e.g. by writing

$$\sum_{l=1}^{L} U_l = 0. \tag{6}$$

We discretize the conductivity σ by approximating it in a piecewise linear basis, and approximate the solution of the CEM, Eqs. (1) - (6), numerically by using the Finite Element Method (FEM) [47, 48]. By further assuming additive Gaussian noise e, the observation model for one set of ERT measurements is written as

$$V = U(\sigma) + e \tag{7}$$

where V is a vector of the measured electrode potentials and $U(\sigma)$ is computational model resulting from the finite element (FE) approximation of the CEM. Here, and below, the spatially distributed conductivity is identified with its finite dimensional approximation σ. Since the conductivity was approximated in the piecewise linear basis, σ consists of nodal values of conductivity in the FE mesh, $\sigma_i, i = 1, \ldots, N$.

2.3. Inverse problem

The inverse problem of ERT is to reconstruct the conductivity distribution σ given the electrode potentials V. Below, in Section 2.3.1, we first review a contemporary reconstruction scheme which can be considered as a modification of Tikhonov regularized solution based on the observation model (7). Previous implementations of the contemporary models used in sensing skin applications specifically refer to the recent works [22, 49, 38]. Next, in Section 2.3.2, the observation models corresponding to states before and after cracking are augmented, and the conductivity change between the states is reconstructed simultaneously with the conducitivity of the intial state using the non-linear difference imaging sceme.

2.3.1. Contemporary reconstruction with approximative model error correction

Based on the observation model (7), the Tikhonov regularized least squares solution can be written in the form [25]

$$\widehat{\sigma} = \arg\min_{\sigma} \{||L_e(V - U(\sigma))||^2 + p(\sigma)\} \tag{8}$$

where L_e is the Cholesky factorization of the noise precision matrix and $p(\sigma)$ is the regularization function, which incorporates prior information, i.e., penalizes unwanted features in σ. We note that since the ERT inverse problem is ill-posed, a (weighted) least-squares solution (corresponding to setting $p(\sigma)$=0) would lead to unstable and non-unique solutions for σ.

When imaging cracking using ERT-based painted sensing skin, the paint surface is rarely uniform, due to practical reasons: They are usually painted either with a paint brush or a pressurized air brush, and in this manual operation, uniformity is very difficult to guarantee. Even if the paint is spread uniformly with some automatic technique, in many surfaces the paint layer may still not be uniform, due to surface roughness or porosity. Consequently, the spatial distribution of the electrical conductivity is usually not uniform, and especially, the conductivity distribution after cracking has a very complex form - featuring

both the variation of the background conductivity of the sensing skin and sharp-edged insulating paths in the locations of the cracks. In [21], the authors simplified the ERT image reconstruction by approximating the background conductivity to be homogeneous, and added a model correction term ϵ in the observation model to account for the errors caused by this approximation. The correction term ϵ was calculated based on reference data V_{ref} measured from the sensing skin prior to cracking

$$\epsilon = V_{\text{ref}} - U(\sigma_{\text{ref}}) \tag{9}$$

where σ_{ref} is a homogeneous estimate for the background conductivity that was obtained by fitting a single parameter representing the constant conductivity to data V_{ref} by solving a least squares problem $\sigma_{\text{ref}} = \arg\min_{\sigma}\{||(V_{\text{ref}} - U(\sigma))||^2\}$, where $\sigma \in \mathbb{R}$.

The contemporary ERT reconstructions using the model error correction are of the form

$$\widehat{\sigma^{\epsilon}} = \underset{0<\sigma\leq\sigma_{\text{ref}}}{\arg\min}\{||L_e(V - U(\sigma) - \epsilon)||^2 + p(\sigma)\}. \tag{10}$$

Here, we have also added constraints ($0 \leq \sigma \leq \sigma_{\text{ref}}$) to the solution, based on the physical fact that electrical conductivity is always non-negative ($\sigma \geq 0$) and the *a priori* information that the changes in the electrical conductivity are solely due to cracking, which can only degrease the electrical conductivity ($\sigma \leq \sigma_{\text{ref}}$). In this paper, the optimization problem (10) is solved iteratively, by the Gauss-Newton method equipped with line-search. The constraints are handled using an interior point method [50], where barrier functions $\bar{f}_k(\sigma_i), i = 1, \ldots, N,\ k = 1, 2$ are added to the function to be minimized. As the barrier functions we use locally supported convex second order polynomial functions $\bar{f}_k(\sigma_i) = \Xi_k(\sigma_i)f_k(\sigma_i)$, where $f_k(\sigma_i)$ is the polynomial and $\Xi_k(\sigma_i)$ is a rectangular function defining the interval $[d_1^{(k)}, d_2^{(k)}]$ where the barrier function is effective (that is, $\Xi_k(\sigma_i) = 1$ when $\sigma \in [d_1^{(k)}, d_2^{(k)}]$ and $\Xi(\sigma_i) = 0$ elsewhere). For example, the non-negativity $\sigma > 0$ is forced by a decreasing segment of a polynomial $\Xi_1(\sigma_i)f_1(\sigma_i)$ in $[d_1^{(1)}, d_2^{(1)}] = [10^{-6}, 10^{-4}]$, where $f_1(\sigma_i) = a_1\sigma_i^2 + b_1\sigma_i + c_1$ and the coefficients a_1, b_1 and c_1 are selected so that the vertex of parabola is at $d_2^{(1)}$ and the value of $f_k(d_1^{(1)})$ is decreased adaptively during the Gauss-Newton iteration. Furthermore, all values $\sigma_i < d_1^{(1)}$ are projected to $d_1^{(1)}$. We note that this choice of barrier function actually limits the value of conductivity to $d_1^{(1)} > 0$, but when $d_1^{(1)}$ is small enough, this approximation has no practical effect on the quality of reconstructions. The reason for the projection in the lower bound is that conductivity values $\sigma \leq 0$ cause numerical problems to the ERT forward solver.

According to Eq. (9), ϵ is the discrepancy between the measured reference data and the modeled data corresponding to homogeneous background conductivity. Thus, ϵ represents the error in the model caused by the homogeneous approximation of the background and possibly some other modeling errors. Substituting ϵ in the solution (10) implies that this error is the same in both measurement sets V_{ref} and V. This, however, is a highly approximative assumption, because in reality, the error in the model output depends on the model unknown, i.e., the conductivity distribution. A rigorous framework to handle this modeling error is referred to as Bayesian approximation error modeling (BAE) [25, 35]. In BAE, the first and second order statistics (mean and covariance) of the modeling error are computed based on sampling, and incorporated in the observation model. Thus, compared with BAE, the approximation made above can be considered as an experimental conterpart of including a zeroth order (constant) correction term into the observation model. Moreover, this approach neglects the contribution of measurement noise in V_{ref}. On the other hand, the advantage of the experimentally based correction is that the zeroth order correction term is obtained without prior knowledge of the factors *causing* the modeling errors. The contemporary reconstructions of the form (10) were shown to provide feasible estimates for the crack patterns in cases where the crack patterns were relatively simple [21]. In the next section, we introduce the non-linear difference imaging approach to ERT-based sensing skin; in this approach, the above approximations are not needed.

2.3.2. Non-linear difference reconstruction

The non-linear difference reconstruction [40] aims at reconstructing the (possibly) non-homogeneous background conductivity of the sensing skin simultaneously with the change of the conductivity based on ERT measuments before and after the change. As above, these data sets are denoted by V_{ref} and V, respectively.

The corresponding conductivity distributions are here denoted by σ_1^s and σ_2^s. [1] We denote the change of conductivity between measurements V_{ref} and V by $\Delta\sigma^s$ Using these notations, we write

$$\sigma_2^s = \sigma_1^s + \Delta\sigma^s. \tag{11}$$

If it is known *a priori* that the conductivity changes in a certain subdomain, or region of interest Ω_{ROI}, we may write $\Delta\sigma^s$ in the form $\Delta\sigma^s = M\Delta\sigma^{s,\text{ROI}}$ where $\Delta\sigma^{s,\text{ROI}}$ is the change of conductivity within Ω_{ROI}, and M is a matrix corresponding an extension mapping $\mathcal{M}$ defined as

$$\mathcal{M}\Delta\sigma^{s,\text{ROI}} = \begin{cases} \Delta\sigma^s, & x \in \Omega_{\text{ROI}} \\ 0, & x \in \Omega \setminus \Omega_{\text{ROI}} \end{cases}. \tag{12}$$

In a case where a region of interest information is not available, we simply choose $\Omega_{\text{ROI}} = \Omega$.

Using the above notations, the observation models corresponding to states before and after cracking can be written as follows

$$\begin{aligned} V_{\text{ref}} &= U(\sigma_1^s) + e_1 \\ V &= U(\sigma_1^s + M\Delta\sigma^{s,\text{ROI}}) + e_2 \end{aligned} \tag{13}$$

where e_1 and e_2 represent the measurement noises in the respective measurements. By concatenating the measurement vectors and observation models, we obtain the block observation model

$$\underbrace{\begin{bmatrix} V_{\text{ref}} \\ V \end{bmatrix}}_{\overline{V}} = \underbrace{\begin{bmatrix} U(\sigma_1^s) \\ U(\sigma_1^s + M\Delta\sigma^{s,\text{ROI}}) \end{bmatrix}}_{\overline{U}(\bar{\sigma^s})} + \underbrace{\begin{bmatrix} e_1 \\ e_2 \end{bmatrix}}_{\bar{e}} \tag{14}$$

which may be written as

$$\overline{V} = \overline{U}(\bar{\sigma^s}) + \bar{e} \tag{15}$$

where

$$\bar{\sigma^s} = \begin{bmatrix} \sigma_1^s \\ \Delta\sigma^{s,\text{ROI}} \end{bmatrix}. \tag{16}$$

Based on the model in Eq. (15), we write the regularized least squares solution as

$$\widehat{\bar{\sigma^s}} = \arg \min_{\substack{\sigma_1^s > \sigma^* \\ \sigma_2^s \geq 0 \\ \Delta\sigma^{s,\text{ROI}} \leq 0}} \{||L_{\bar{e}}(\overline{V} - \overline{U}(\bar{\sigma^s}))||^2 + p(\bar{\sigma^s})\} \tag{17}$$

where $p(\bar{\sigma^s})$ is the compound regularization functional and $L_{\bar{e}}$ is the Cholesky factor of the noise precision matrix (see below). In selecting the constraints on σ_1^s, $\Delta\sigma^{s,\text{ROI}}$, and σ_2^s, we use *a priori* information: As in the contemporary solution (10), the conductivity of the damaged sensing skin, σ_2^s, is known to be non-negative, and the conductivity change, $\Delta\sigma_1^{s,\text{ROI}}$, is known to be non-positive. In addition, a constraint for the background conductivity σ_1^s is written; in Eq. (17), $\sigma^* \geq 0$ is the lower bound for σ_1^s. We note that the presence of σ^* is useful in limiting artifacts resulting from cross-talk between reconstructions of σ_1^s and $\Delta\sigma_1^{s,\text{ROI}}$, as noted in [40]. All the constraints of problem (17) were handled with the same interior point method as those in problem (10), with obvious modifications of the second order polynomial barrier functions depending on the values of the limit points.

Above, matrix $L_{\bar{e}}$ is defined as: $L_{\bar{e}}^T L_{\bar{e}} = \Gamma_{\bar{e}}^{-1}$ where the block form of $\Gamma_{\bar{e}}$ is

$$\Gamma_{\bar{e}} = \begin{bmatrix} \Gamma_{e_1} & \mathbf{0} \\ \mathbf{0} & \Gamma_{e_2} \end{bmatrix} \tag{18}$$

[1] We note that conductivities before and after cracking, σ_1^s and σ_2^s, correspond to σ_{ref} and σ above. Here we use subindices 1 and 2 to emphasize that the conductivity is spatially distributed both before and after cracking, while above σ_{ref} was homogeneous. Secondly, the superscript s is used for indicating that in the non-linear difference imaging, the conductivities are reconstucted based on a *stacked* (augmented) model.

Further, we assume a stationary model of the noise statistics, and write $\Gamma_{e_1} = \Gamma_{e_2}$. The regularization functional $p(\bar{\sigma^s})$ carries prior information and penalizes undesirable features of $\bar{\sigma^s}$. The compound regularization functional, $p(\bar{\sigma^s})$, is written as

$$p(\bar{\sigma^s}) = p_{\sigma_1}(\sigma_1^s) + p_{\Delta\sigma}(\Delta\sigma^{s,\mathrm{ROI}}) \tag{19}$$

which allows for different regularization functionals, p_{σ_1} and $p_{\Delta\sigma}$, to provide prior information regarding the spatial distribution of σ_1^s and $\Delta\sigma^{s,\mathrm{ROI}}$, respectively. This is of particular importance in relating this reconstruction scheme to the physics of mechanically-induced damage. In characterizing the conductivity distribution prior to cracking, we describe $p_{\sigma_1}(\sigma_1^s)$ using smoothness promoting regularization

$$p_{\sigma_1}(\sigma_1^s) = ||L_{\sigma_1}(\sigma_1^s - \eta_{\sigma_1})||^2 \tag{20}$$

where L_{σ_1} is regularization matrix defined as in [40] and η_{σ_1} is the expected value of σ_1^s which is here chosen to be equal to σ_{ref}, homogeneous estimate for the background conductivity, see Section 2.3.1. For the change in conductivity, $\Delta\sigma^{s,\mathrm{ROI}}$, (caused by cracking) we utilize the isotropic total variation (TV) regularization [51]

$$p_{\Delta\sigma}(\Delta\sigma^{s,\mathrm{ROI}}) = \alpha \sum_{k=1}^{N_e} \sqrt{||(\nabla\Delta\sigma^{s,\mathrm{ROI}})|_{e_k}||^2 + \beta} \tag{21}$$

where α is the TV weighting parameter, $(\nabla\Delta\sigma^{s,\mathrm{ROI}})|_{e_k}$ is the gradient of $\Delta\sigma^{s,\mathrm{ROI}}$ at element e_k, β is a stabilization parameter, and N_e is the number of elements in the FE mesh corresponding to subdomain Ω_{ROI}. This choice for $p_{\Delta\sigma}(\Delta\sigma^{s,\mathrm{ROI}})$ promotes sharp edges in the spatial distribution of the conductivity change $\Delta\sigma^{s,\mathrm{ROI}}$, which is a realistic assumption when $\Delta\sigma^{s,\mathrm{ROI}}$ is caused by cracking. Parameters used in the ERT reconstructions are listed in Table 1.

When estimating the solution of Eq. (17) using a Gauss-Newton iteration, the Jacobian matrix of $\overline{U}(\bar{\sigma^s})$ is required. The Jacobian, $J_{\overline{U}}(\bar{\sigma^s}) = \frac{\partial\overline{U}}{\partial\bar{\sigma^s}}$, is given by [40]

$$J_{\overline{U}}(\bar{\sigma^s}) = \begin{bmatrix} J_U(\sigma_1^s) & \mathbf{0} \\ J_U(\sigma_1^s + M\Delta\sigma^{s,\mathrm{ROI}}) & J_U(\sigma_1^s + M\Delta\sigma^{s,\mathrm{ROI}})M \end{bmatrix} \tag{22}$$

where $J_U(\sigma)$ is the Jacobian of the mapping $U(\sigma)$ [52], and $\mathbf{0}$ denotes an all-zero matrix. In the constrained optimization problem (Eq. 17), the Gauss-Newton algorithm is equipped with line search.

The use of non-linear difference reconstruction has the following advantages: First, it allows for incorporating different type of prior information on the spatial properties of the background conductivity and the conductivity change. This is an appealing feature, when the conductivity change is caused by cracking while the spatial variation in the background conductivity is mainly due to variation in the thickness of the paint layer. Secondly, in cases where the conductivity change is known *a priori* to happen in a region of interest, restricting the solution to this subdomain can improve the reconstructions significantly [40]. This restriction also reduces the computational cost, because it decreases the number of unknowns in the model. Finally, in [41], the non-linear difference reconstructions were shown to tolerate systematic modeling errors (such as inaccuracies in the model geometry and contact impedances) even better than convential linearized difference reconstructions.

3. Using a structural model to obtain prior information in ERT

In this work, we select the region of interest, Ω_{ROI}, for ERT by numerically modeling the structures of interest. Two structural configurations are investigated herein, both are reinforced concrete beams with different geometries, material parameters, reinforcement schemes, and support/loading configurations. Since we are only interested in detecting cracking, our intended Ω_{ROI} corresponds to the potentially cracked areas of the beams.

To determine Ω_{ROI}, we began by conducting finite element modeling of the target geometries. In doing this, we employed the open source FEM software FormWorks [53]. In the analysis, material properties, beam geometry, reinforcement detailing, and loading conditions were input as model parameters. For the elastic and post-cracking concrete material model we utilized the model from [39] and considered zero-slip conditions for the steel reinforcement. After obtaining the simulation results, the region of highest cracking

probability was determined from open source post-analysis software Janus [54]. A simple criteria was used to determine the region of highest cracking probability: any element with a principle tensile stress f_p greater than the concrete tensile strength f_t, i.e. $\Omega_{\text{ROI}} = \Omega(f_p > f_t)$. The tensile strength f_t was estimated as $f_t = 0.7\sqrt{f_c'}$ (MPa), which was taken as the split-cylinder strength for normal weight concrete from the ACI building code [55]. This criteria results in growth of Ω_{ROI} with increasing load.

Using image analysis, the images including areas of probable cracking were converted to binary form. Finally, Ω_{ROI} was determined by superimposing binary values of the cracked section onto the mesh used during ERT inversion. A schematic describing the generation of Ω_{ROI} is shown in Fig. 2, and the selected regions of interest, Ω_{ROI}, for all beam geometries are reported in Section 4.

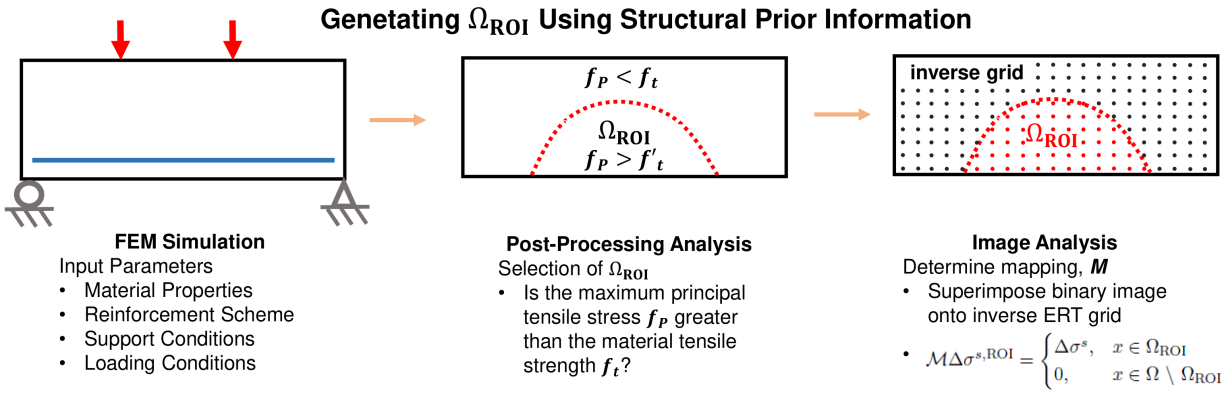

Figure 2: Schematic illustrating the generation of Ω_{ROI}.

We would like to remark that the FEM model used to determine the principal stresses in the beam accounts for the non-linear mechanical behavior of concrete, the dimensions of the beam, the location of the reinforcement, the non-linear mechanical behavior of reinforcement, and the bond behavior. Since estimations of Ω_{ROI} should be conservative (i.e. Ω_{ROI} should always be equal to or larger than the region containing cracks to avoid significant artifacts in reconstructions of σ within Ω_{ROI}), it may not be advisable to use simplified models often obtained using empirical or analytical expressions that do not account for all structural parameters.

4. Experimental and simulation studies

The ability of ERT to image complex cracking patterns was investigated both experimentally and numerically. While the experimental study demonstrates the feasibility of ERT to image cracks in a realistic measurement setup, the numerical simulation studies allow for testing the effects of various factors in the quality of ERT based crack detection. Especially, the effects of crack pattern complexity and background conductivity variation (i.e., the variation of the paint layer thickness) are studied. In all cases, we compare the ERT reconstructions computed with the contemporary method (Section 2.3.1) and non-linear difference reconstruction (Section 2.3.2) with and without region of interest information provided by the structural model discussed in Section 3.

4.1. Experimental study

4.1.1. Experimental ERT data from a mortar beam

For the experimental study, data from a recent work [22] was used. This data was collected from a reinforced concrete beam that was progressively loaded in three-point bending while a corrosive agent penetrated the material. Two sensing skins with 28 electrodes were applied to the beam with a polymeric electric insulator between the layers. One layer (copper sensing skin) was designed to detect corrosion and cracking, while the other layer (silver sensing skin) detected only cracking. In the present paper, we used the data from the silver layer only, as we focused on the crack detection.

The beam geometry was 152 mm × 508 mm × 152 mm (H × L × D). Minimal tensile steel reinforcement was used, with a reinforcement ratio of $\rho = 0.1\%$ at a depth of $d = 112$ mm. No transverse reinforcement was used. A 35 mm deep notch was cast in the bottom of the beam to initiate localized cracking in the center. The compressive strength f'_c was not measured, however given the curing conditions and mixture properties, the compressive strength was estimated as $f'_c = 30$ MPa. These structural properties are listed in Table 1.

The beam was loaded until failure which occured at 21.8 kN. A total of twelve sets of ERT measurements were collected at different stages of loading. For this study, we selected three of these measurement sets (11.6, 16.9, and 21.8 kN), because between these loads, the cracks clearly progressed on the beam surface, and thus these measurements represent stages with different levels of crack complexity (where "level" refers to the cracking pattern at each loading state). Photographs of the cracking patterns are provided in Section 5 (see Fig. 7, left column). Based the material properties, beam geometry, reinforcement scheme, and loading conditions, areas of with high probability for cracking were identified by using the FormWorks software, as described in Section 3. The progress of this area (used as region of interest Ω_{ROI} in ERT) is illustrated in Fig. 3. The regions of interest Ω_{ROI_1}, Ω_{ROI_2} and Ω_{ROI_3} correspond to loads 11.6, 16.9, and 21.8 kN, respectively. We note that the regions of interest shown in Fig. 3 are not exactly symmetric with respect to the vertical axis at the center of the beam; the small shift to the right is a result of a slight eccentricity in the applied load.

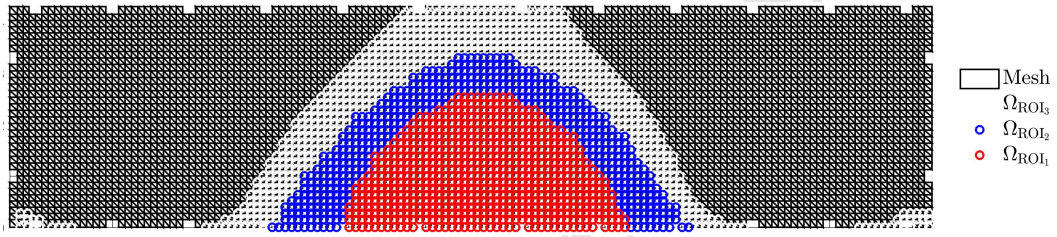

Figure 3: Regions-of-interest for the experimentally-tested beam superimposed on the inverse mesh. Ω_{ROI_1} (red) corresponds to the lowest level of cracking, Ω_{ROI_2} (blue) corresponds to the intermediate level of cracking, and Ω_{ROI_3} (white) corresponds to the highest level of cracking.

4.1.2. Experimental ERT measurements and reconstruction

ERT measurements were taken using in-house equipment with a measurement precision of 1.0×10^{-8} V. A total of 54 1.0 mA DC current injections were applied between electrodes i and j, $i = 6, 21$ and $j = 1, ..., 28, i \neq j$. Corresponding to each current injection, adjacent electrode potentials were measured with respect to a common ground. This scheme resulted in 1458 ERT measurements.

In the FE approximation of the ERT forward model (Section 2.2), an approximately uniformly-distributed triangular mesh consisting of $N_n = 9{,}680$ triangular elements and $N_e = 5{,}047$ nodes was used. Hence, in the piecewise linear approximation of the unknown conductivity distribution, vectors representing nodal values of conductivity consisted of 5,047 entries. The ERT FE mesh is shown in Fig. 3.

4.2. Simulation study

To test the feasibility of ERT to detect complex and dense cracking patterns, and to study the effect of inhomogeneity in the background conductivity, a simulation study was conducted. In this study, imaging of three crack patterns was considered, each of them in cases of four different distributions of the background conductivity on the sensing skin. The models for cracks were adopted from [56], where complex cracks patterns were formed in a reinforced concrete beam by loading it progressively.

4.2.1. The modeled beam

The simulation beam geometry was 400 mm × 3000 mm × 200 mm (H × L × D). The beam was lightly reinforced (flexural reinforcement ratio $\rho = 1.0\%$, reinforcement depth $d = 360$ mm), without transverse reinforcement. For this beam, the compressive strength f'_c was taken directly from article [56], and f_t was estimated in the same manner as the experimental beam. The properties are listed in Table 1. Four-point loading was used with a spacing of $1.5d$ between loading points. The failure load was approximately 171.4 kN. The loading, geometry, and reinforcement scheme were designed to induce diagonal flexural-shear cracking.

The cracking patterns near failure were dense with complex geometries and were therefore deemed suitable for this study. Three load cases from this study showing clear visual progression of cracks were selected: 51.4, 137.1, and 171.4 kN. The selected three cracking patterns are shown in Fig. 8 (left column) in the results section.

Table 1: Experimental and simulated beam parameters

	Geometry			Material		Reinforcement		ERT	
	L(mm)	H(mm)	D(mm)	f'_c (MPa)	f_t (MPa)	ρ (%)	d (mm)	σ^*	β^2
Experimental	475	152	152	30.0	3.8	0.1	112	$0.5\sigma_{\text{ref}}$	$0.1(\frac{\sigma_{\text{ref}}}{w_e})^2$
Simulation	3000	400	200	53.7	5.1	1.0	360	$0.5\sigma_{\text{ref}}$	$0.1(\frac{\sigma_{\text{ref}}}{w_e})^2$

4.2.2. Sensing skins, measurement simulation and reconstructions

To test the sensitivity of ERT to sensing skin inhomogeneity, four background conductivities (conductivities of the undamaged sensing skins) were used. These distributions were i) homogeneous conductivity of 10 S, ii) ellipsoidal inclusion with a conductivity range of 10-15 S (increasing toward the center), iii) ellipsoidal inclusion with a conductivity range of 5-10 S (decreasing toward the center), and iv) randomized "blob-like" conductivity distribution with a range of 5-15 S. [3] The above ranges of conductivity values were approximated from sensing skins used in previous experimental studies. The spatial variations of backround conductivity in Cases (i)-(iv) represent different levels of complexity and realism: While the homogeneous background (Case (i)) is expected to be the most feasible setting for the crack detection, it may be very difficult to physically implement, especially in the large scale case. In Cases (ii) and (iii), the background conductivity values have a large range, but they change symmetrically with respect to the central axis, and the spatial dimensions of the inhomogeneities are very large, which may not be the case in a real large scale sensing skin setup. Thus, Case (iv) featuring non-symmetrically distributed spatial variation of the background conductivity is expected to represent the most realistic situation of a painted sensing skin. The background conductivities are shown in Fig. 4.

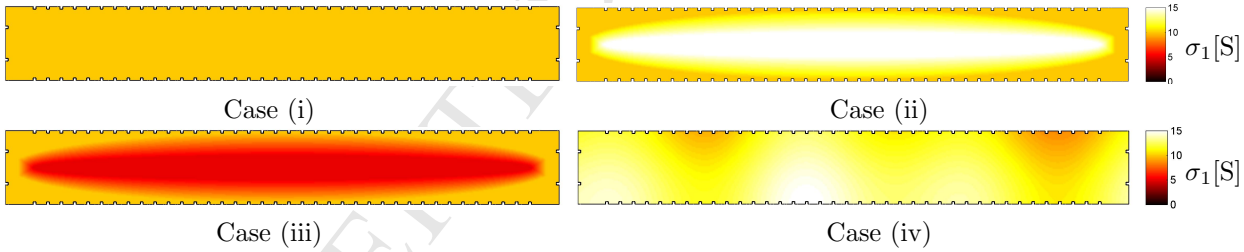

Figure 4: Simulated conductivity σ_1 of undamaged sensing skins. Case (i): homogeneous conductivity, Case (ii): ellipsoidal inclusion with increasing conductivity towards the center, Case (iii): ellipsoidal inclusion with dereasing conductivity towards the center, and Case (iv): randomized blob-like conductivity.

In cases of all four background conductivities (Cases (i)-(iv)), detection of same three crack patterns (see above) was studied. In the simulations, the cracks were considered as electrically insulating patterns [21], i.e., when mapping the crack patterns adopted from [56] to the ERT FE mesh, the conductivity values associated with FE mesh nodes in the locations of cracks were set to close to zero (10^{-6} S).

To simulate ERT measurements, a dense FE mesh with $N_n = 43,032$ nodes and $N_e = 22,142$ triangular elements was used. A total of 80 electrodes with contact impedances of $z_0 = 1.0 \times 10^{-5}$ Ωm were modeled, and 79 DC current injections of magnitude 1.0 mA corresponding to 6,320 adjacent potential measurements

[2] w_e denotes the width of the finite element.

[3] Here, we note that since the models are two dimensional, σ represents the two-dimensionally distributed surface conductivity of the thin paint layer. The unit of 2D conductivity is S, as opposed to S/m, the unit of conductivity in 3D.

were simulated. Following data simulation, Gaussian noise with standard deviation 0.5% of the corresponding measurement value was added to the measurements.

When solving the ERT inverse problem, a more coarse FE mesh was used. The uniformly-distributed triangular mesh consisted of $N_n = 10,964$ triangular elements and $N_e = 5,796$ nodes. The resulting ERT inverse mesh is shown in Fig. 5 with the regions of interest shown atop the mesh (cf. Section 3 for determining Ω_{ROI}). The resulting unknown conductivity vector consisted of 5,796 entries. ERT reconstruction parameters for the simulation study are provided in Table 1.

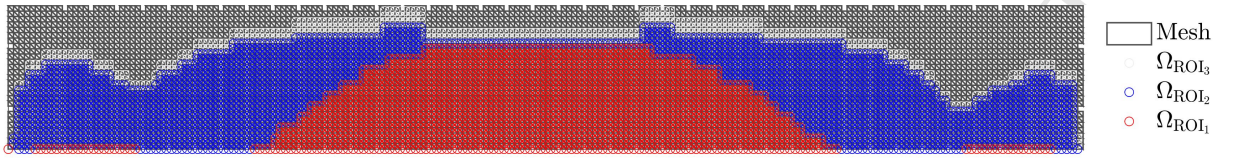

Figure 5: Regions-of-interest for simulation beam superimposed on the coarse inverse mesh. Ω_{ROI_1} (red) corresponds to the lowest level of cracking, Ω_{ROI_2} (blue) corresponds to the intermediate level of cracking, and Ω_{ROI_3} (white) corresponds to the highest level of cracking.

4.3. Identification and visualization of crack patterns

When the contemporary reconstruction scheme (Section 2.3.1) is used, the background conductivity is approximated to be homogeneous, and the errors caused by this approximation are modeled by the error term ϵ. In our previous works [15, 22], this approximation was adequate, and the cracks were identified feasibly by $\widehat{\sigma^{\epsilon}}$: these estimates showed very low conductivities in the locations of the cracks, while the values were near to constant σ_{ref} elsewhere, despite some imaging artifacts. In the non-linear difference imaging scheme, however, the identification and visualization of cracks is slightly more problematic: When the background conductivity is inhomogeneous, the estimate for the conductivity in the cracked state σ_2^s (counterpart of $\widehat{\sigma^{\epsilon}}$) shows also the background inhomogeneities. On the other hand, illustrating the estimated change of conductivity, $\Delta\sigma^{\mathrm{s}}$, should show change only in the locations of the cracks, and could in principle used for identifying the cracks. However, depending on the spatial variation of the background conductivity, the values $\Delta\sigma^{\mathrm{s}}$ corresponding to cracked state may vary significantly, and this could make the $\Delta\sigma^{\mathrm{s}}$ -based identification of cracks obscure and prone to reconstruction artifacts. For these reasons, we choose to identify the cracks based on the (spatial distribution of) the normalized value $\sigma_{\mathrm{n}} = \frac{\sigma_2}{\sigma_1}$. Indeed, σ_{n} should reflect the magnitude of the local damage on the sensing skin even if the background is inhomogeneous: in any location, the value $\sigma_{\mathrm{n}} = 0$ corresponds to fully cracked state ($\sigma_2 = 0$), while $\sigma_{\mathrm{n}} = 1$ indicates an intact location on the sensing skin as it corresponds to the case $\sigma_2 = \sigma_1$.

In the next section we thus visualize the simulated crack patterns by illustrating images of σ_{n}. Correspondingly, the crack patterns estimated by non-linear difference imaging are illustrated by depicting $\sigma_{\mathrm{n}}^{\mathrm{s}} = \frac{\sigma_2^{\mathrm{s}}}{\sigma_1^{\mathrm{s}}}$. The respective normalized estimate using the region of interest based on structural modeling is denoted by $\sigma_{\mathrm{n}}^{\mathrm{s,ROI}}$. To make the comparison clear we similarly illustrate the contemporary reconstructions by visualizing $\sigma_{\mathrm{n}}^{\epsilon} = \frac{\sigma^{\epsilon}}{\sigma_{\mathrm{ref}}}$. Note that since the cracks are the only changes between the states σ_1 and σ_2, and the cracks are insulating, the true values σ_{n} are of binary form (either 0 or 1 for each value of σ_{n}). The estimates $\sigma_{\mathrm{n}}^{\mathrm{s}}$ and $\sigma_{\mathrm{n}}^{\epsilon}$, on the other hand, are not restricted to binary values; however, they are bound between 0 and 1 due to the constraints in the associated estimates for σ_1 and σ_2 (cf. Section 2.3).

Fig. 6 illustrates the reconstructed quantities in non-linearized difference imaging by an example from the experimental study. The two leftmost images represent the primary unknowns of the inverse problem: the initial (background) conductivity, σ_1^{s}, and the conductivity change due to cracking, $\Delta\sigma^{\mathrm{s}}$. The third image shows $\sigma_2^{\mathrm{s}} = \sigma_1^{\mathrm{s}} + \Delta\sigma^{\mathrm{s}}$, the estimate for the conductivity distribution after cracking. This example demonstrates that interpreting the crack pattern solely based on σ_2^{s} is difficult, as the background conductivity has a lot of variation. However, the fourth image which illustrates $\sigma_{\mathrm{n}}^{\mathrm{s}} = \frac{\sigma_2^{\mathrm{s}}}{\sigma_1^{\mathrm{s}}}$ reveals the crack pattern clearly.

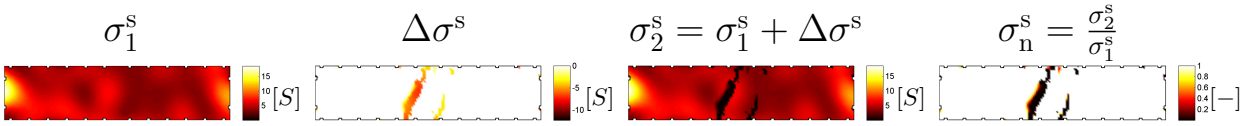

Figure 6: An example of reconstructed quantities in non-linearized difference imaging. Far left column: reconstruction of undamaged sensing skin σ_1^{s}, second column: reconstruction of the conductivity change due to cracking $\Delta\sigma^{\mathrm{s}}$, third column: the conductivity of the damaged sensing skin σ_2^{s}, and the fourth column: normalized conductivity $\sigma_{\mathrm{n}}^{\mathrm{s}}$.

5. Results and discussion

5.1. Experimental study

Fig. 7 shows results from the experimental case, i.e., the beam loaded mechanically in three-point bending. The results of three loading conditions are reported (11.6, 16.9, and 21.4 kN), which correspond to increasing complexity of cracking patterns. The figure shows photographs of a damaged beam with three cracking patterns, contemporary reconstructions based on the approximate modeling error term ($\sigma_{\mathrm{n}}^{\epsilon}$), and reconstructions based on non-linear difference imaging without and with structural region-of-interest information ($\sigma_{\mathrm{n}}^{\mathrm{s}}$ and $\sigma_{\mathrm{n}}^{\mathrm{s,ROI}}$, respectively).

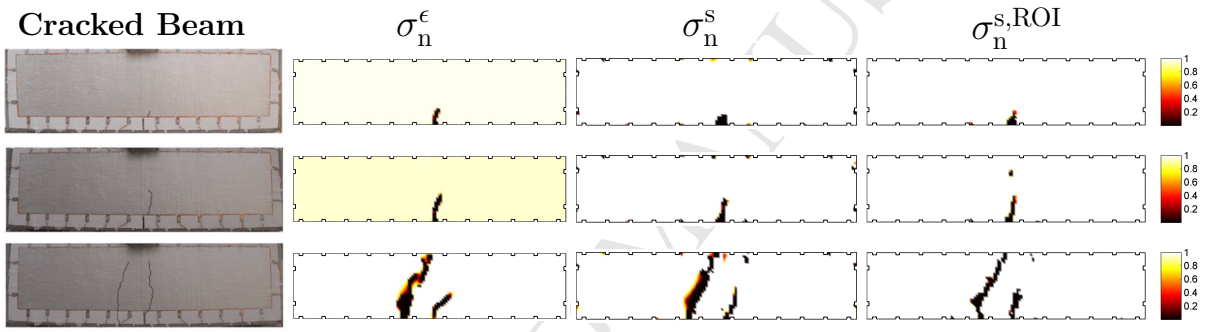

Figure 7: Results of the experimental study. The far left column shows photographs of the cracked beams, column 2 shows the reconstructions reporting normalized conductivity for the contemporary method, and columns 3 and 4 correspond to non-linear difference imaging without and with structural region-of-interest information.

At early stages of cracking (first two rows in Fig. 7), all reconstructions capture the location and approximate geometry of the cracks from experimental data. The observed similarity in the reconstructions' accuracy at early stages of cracking results from the single localized change in conductivity between boundary electrodes, a cracking state which is especially well suited for detection using ERT [22]. Also in the final cracking stage, all reconstructions perform relatively well. However, the contermporary reconstruction (bottom row, 2nd column) slightly misrepresents the geometry of both cracks, and on the other hand, the use of use of structural region-of-interest information ($\sigma_{\mathrm{n}}^{\mathrm{s,ROI}}$, bottom row, 4th column) slightly improves the resolution.

The results of the experimental study demonstrate the feasibility of the non-linear difference reconstruction, a novel computational method that was introduced to the sensing skin application in this paper. However, since the differences between the qualities of different reconstructions are very small, the results do not yet justify drawing conlusions on the potential advantage of the non-linear difference reconstruction over the contemporary reconstruction method. To compare the performances of different reconstruction methods in cases of complex crack patterns, simulation studies were carried out. In these studies, the sensitivity of different reconstructions to inhomogeneity in background conductivity was also investigated. The results of these studies are shown in the next section.

5.2. Simulation study

The results of the simulation studies are shown in Fig. 8. The left column of the figure shows the true crack patterns in the form of normalized conductivity distribution σ_{n} in cases of four different background

conductivity distributions σ_1 illustrated in Fig. 4. Note that since the crack patterns are defined in the same manner in all four cases (assigning $\sigma_2 = 0$ in the locations of cracks and $\sigma_2 = \sigma_1$ elsewhere), the distributions σ_n corresponding to each crack pattern are mutually equal in all cases, despite the differences in the background conductivities. The reconstructed distributions σ_n^ϵ, σ_n^s and $\sigma_n^{s,ROI}$ and shown in columns 2-4.

In Case (i), where the background conductivity was homogeneous, the contemporary, approximative error model-based estimate σ_n^ϵ shows the simplest crack pattern with a good resolution; all four cracks are well detected and localized, and their lengths can be assessed based on the reconstructed image. The background conductivity, however, is somewhat incorrectly estimated, as in this image, all values of σ_n^ϵ are slightly below 1, indicating a small negative change in the whole sensing skin between states σ_1 and σ_2. In the second level of cracking where the crack pattern is more complex (Case (i), second row), σ_n^ϵ estimates the pattern with slightly lower accuracy. The large cracks are again detected but the resolution does not allow for distinguishing the smallest cracks. Moreover, the values outside cracks are even further below 1. Similarly, in the third stage of cracking, the values of σ_n^ϵ in the areas of the largest cracks are close to zero, but the fine details of the pattern are missed, and image shows, erroneously, even larger overall change of conductivity in the entire area of the sensing skin.

In Cases (ii), (iii) and (iv), the contemporary estimate σ_n^ϵ shows the crack pattern roughly in the same accuracy as in Case (i), yet the accuracy is clearly worst in Case (iii). The difference between Cases (ii) and (iii) is explained by the difference in the conductivity contrasts caused by the cracking. Indeed, in Case (ii), the background conductivity σ_1 is high (15 S) in the central area where majority of the cracks occur (cf. Fig. 4), while in Case (iii), σ_1 is only about 5 S the same area; hence, the higher conductivity contrast of Case (ii) between the background and the cracks enables better resolution of cracks. Also in Case (iv), where the overall conductivity contrast is high, yet σ_1 is non-symmetrically distributed, the resolution of cracks is better than in Case (iii).

The results obtained using the contemporary, approximative error model -based reconstruction thus show that the accuracy of σ_n^ϵ drops when the crack pattern gets more complex – this is supported by all simulation cases: the simplest crack patterns are detected with best accuracy in all backgrounds. We also note that in the simulations, all crack patterns are more complex than in the experimental case, where the number of cracks was two; consequently, the resolution of all simulation based reconstructions σ_n^ϵ is somewhat lower than in the experimental case. Based on the above observations – especially those related to differences between Cases (ii) and (iii) – it is also apparent that the quality of the contemporary reconstructions depends on the background conductivity distribution.

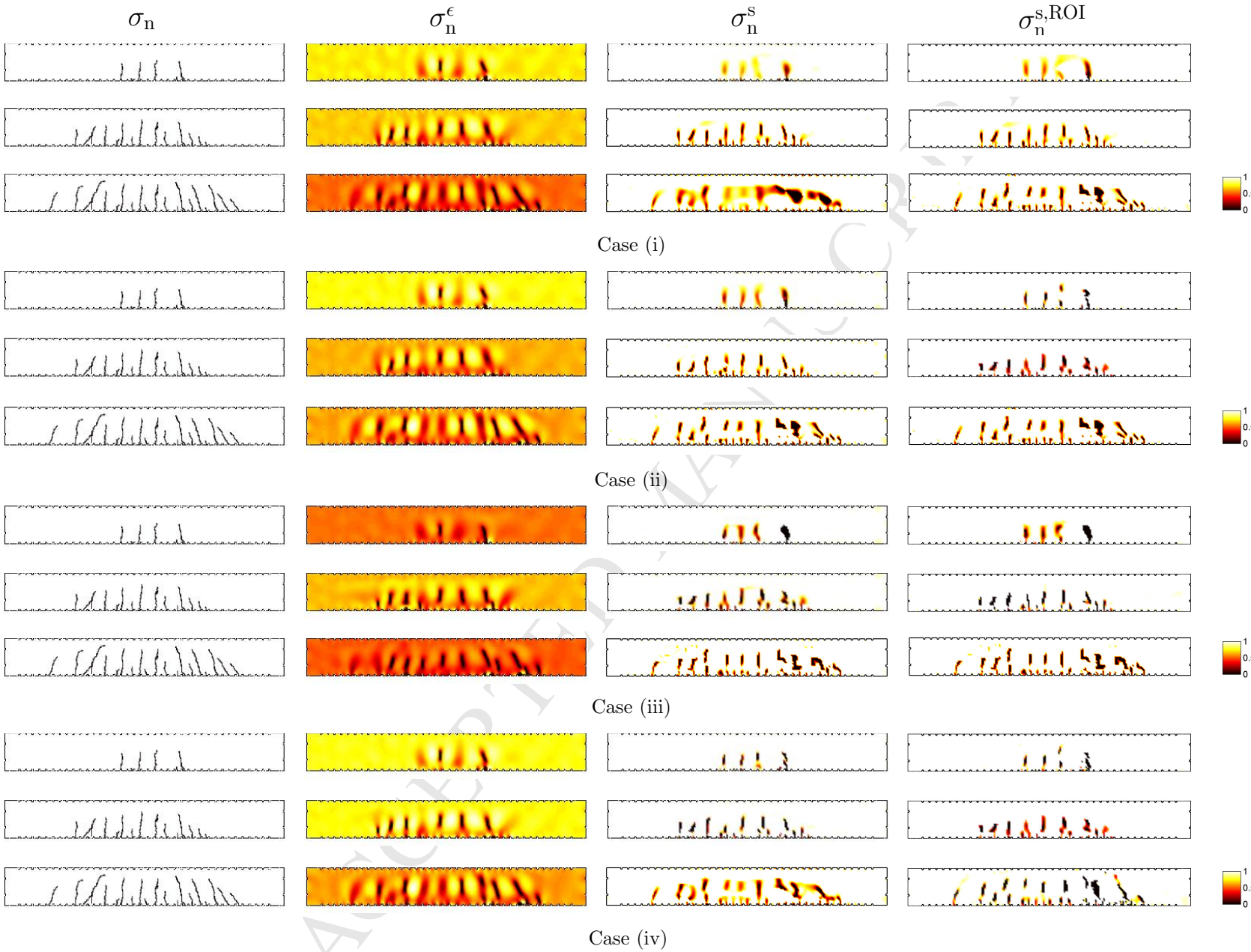

Figure 8: Results of the numerical simulations. Left column: Simulated (true) cracking patterns represented in the form of normalized conductivity distributions σ_{n}. Columns 2-4: normalized conductivity distributions $\sigma_{\mathrm{n}}^{\epsilon}$, $\sigma_{\mathrm{n}}^{\mathrm{s}}$ and $\sigma_{\mathrm{n}}^{\mathrm{s,ROI}}$ corresponding to three reconstruction methods. The results on imaging the evolution of the crack pattern (three different patterns) are shown in cases of four different background conductivity distributions σ_1: Case (i) homogeneous background; Case (ii), ellipsoidal inclusion with increasing conductivity towards the center; Case (iii), ellipsoidal inclusion with decreasing conductivity towards the center; and Case (iv), spatially smooth, randomized background.

The effect of the crack complexity on the quality of σ_n^ϵ is intuitively appealing, and the reason is twofold: First, since ERT is a diffusive imaging modality, its resolution is generally low; the experimental results in Fig. 7 represent a case of exceptionally high resolution. Obviously, when the crack pattern gets more complex, solving the ERT inverse problem is more challenging, and the resolution is expected to be lower. Secondly, when the crack pattern increases in complexity, the approximation behind the error model also becomes worse – as noted in Section 2.3.1, substituting the error term ϵ in the solution (10) implies that the error is the same in both measurement sets V_{ref} and V. Due to non-linearity of the ERT model, however, the this assumption is approximative, and it becomes increasingly inaccurate when the conductivity difference between the two states increases – for example in the case of increasingly complex crack patterns. Here, we note that the approximative error term ϵ accounts for the effects of *all* modeling errors in the output of the forward model. In Cases (ii)-(iv), it is apparent that approximating the spatially distributed background conductivity by a constant value causes a large error. However, modeling errors are present also in Case (i), because the assumed conductivity σ_{ref} is only an estimate for the constant background conductivity σ_1, not its actual values. Moreover, in all cases (i)-(iv), the coarse discretization of the model used in the inversion results in another modeling error which is, implicitly, included in the error term ϵ, and as discussed above, the feasibility of this approximation is gets worse when the crack pattern gets more complex. Also the dependence of the quality of σ_n^ϵ on the background conductivity is intuitive, based on the above observations on differences in the conductivity contrasts between different cases, and due to its effect on the approximative error model.

The performance of the non-linear difference reconstruction -based estimates σ_n^s and $\sigma_n^{s,\text{ROI}}$ differs significantly from that of σ_n^ϵ. In Case (i), both σ_n^s and $\sigma_n^{s,\text{ROI}}$ reveal the crack patterns clearly in all stages of cracking. Especially the reconstructions $\sigma_n^{s,\text{ROI}}$ have a good resemblence with the true crack pattern; in the case of the most complex crack pattern, the image of σ_n^s is more blurred than $\sigma_n^{s,\text{ROI}}$. This difference is explained by the region-of-interest information included in $\sigma_n^{s,\text{ROI}}$: In σ_n^s , where the change of conductivity is not restricted to a region-of-interest, a number of small artifacts appear in the neighborhood on the topmost electrodes; despite the small size of these artifacts, they have a significant impact on the crack pattern, because of the high sensitivity of ERT data to changes near electrodes. Thus, the additional *a priori* information provided by the structural modeling improves the reconstructions.

In Cases (ii)-(iv), the qualities of σ_n^s and $\sigma_n^{s,\text{ROI}}$ are very similar to those in Case (i). Again, these reconstructions have much better resolution than σ_n^ϵ, and in the cases of complex crack patterns, the region-of-interest based reconstructions $\sigma_n^{s,\text{ROI}}$ are slightly more accurate than σ_n^s.

Also the region-of-interest based reconstructions $\sigma_n^{s,\text{ROI}}$ miss some of the finest details of the most complex crack pattern. This is again due to resolution limit of ERT. In addition to above mentioned effect of the diffusive nature of the imaging modality, there is also a shielding effect caused cracking: In cases where more than two cracks occur between a neighbouring pair of electrodes, the measurement data does not carry enough information to separate those cracks. This problem, of course, could be diminished by increasing the number of electrodes. Nevertheless, taking into account the typical limitations ERT, the reconstructions based on non-linearized difference imaging are able to capture the crack pattern relatively well.

The results demonstrate that ERT-based sensing skins are able to reconstruct and detect complex crack patterns, when non-linearized difference imaging is used, especially when the structural modeling -based region of interest information is incorporated into the reconstructions. Moreover, the variation of the background conductivity has practically no effect on the reconstructions using non-linearized difference imaging. This is an appealing feature, as in a practical setup, it may be difficult to apply sensing skin evenly on the monitored surface.

6. Conclusions

Electrical Resistance Tomography (ERT) imaging of solid materials and structures has recently drawn a lot of attention in research. Especially, the applicability of ERT-based surface sensing systems, or sensing skins, to image cracks and other defects has been studied extensively. However, thus far only relatively simple-formed defects have been considered, and it has been an open question, whether electrical imaging could be used to detect complex structural cracking patterns. Our study focused on finding an answer to this question.

The ability of ERT to detect and reconstruct complex cracking patterns was tested experimentally and by numerical simulations. In the latter studies, the effect of the background conductivity of the sensing skin was also investigated. To improve the resolution of ERT, we adopted a novel, non-linear difference imaging -based reconstruction method to sensing skin. Furthermore, we demonstrated how to include stuctural modeling -based region-of-interest information in the ERT reconstructions.

As expected, adding complexity to the crack pattern and background conductivity distribution make imaging the crack pattern more challenging, and the contemporary reconstruction scheme used successfully in the previous studies fails to detect the most complex patterns. The use of non-linear difference imaging improves the resolution significantly, and by incorporating the region-of-interest information the resolution can be further improved. In addition, the non-linear difference imaging -based crack pattern estimates were found to tolerate the spatial variation of the sensing skin's background conductivity very well. The results demonstrate that ERT is capable of imaging complex structural cracking patterns. This finding extends the potential of electrical imaging -based surface sensing systems, as in many applications where crack detection is needed, the crack patterns can have a complex structure.

Acknowledgments

This work was conducted at the Department of Applied Physics at the University of Eastern Finland supported by a United States Fulbright Grant. The third author would like to acknowledge the support provided by Academy of Finland (projects 270174 and 303801, and the Centre of Excellence in Inverse Problems Research). Computations were carried out using the High-Performance Computing (HPC) Load-Sharing Facility (LSF), a service provided by the NCSU Office of Information Technology (OIT). In addition, the authors acknowledge the expertise from Dr. Gary Howell and Dr. Jianwei Dian for the technical assistance in using the LSF environment. All support is greatly acknowledged.

References

[1] S. Rehman, Z. Ibrahim, S. A. Memon, M. Jameel, Nondestructive test methods for concrete bridges: A review, Construction and Building Materials 107 (2016) 58 – 86.

[2] Z. P. Bažant, L. Cedolin, Stability of structures: elastic, inelastic, fracture and damage theories, World Scientific, 2010.

[3] S. Mindess, J. F. Young, D. Darwin, Concrete, Prentice Hall, 2003.

[4] S. T. Rolfe, J. M. Barsom, Fracture and fatigue control in structures: applications of fracture mechanics, ASTM International, 1977.

[5] L. Rippert, M. Wevers, S. Van Huffel, Optical and acoustic damage detection in laminated CFRP composite materials, Composites science and technology 60 (14) (2000) 2713–2724.

[6] J. Kang, Y. Ososkov, J. D. Embury, D. S. Wilkinson, Digital image correlation studies for microscopic strain distribution and damage in dual phase steels, Scripta Materialia 56 (11) (2007) 999–1002.

[7] L. Yu, V. Giurgiutiu, In situ 2-D piezoelectric wafer active sensors arrays for guided wave damage detection, Ultrasonics 48 (2) (2008) 117–134.

[8] S. S. Kessler, S. M. Spearing, C. Soutis, Damage detection in composite materials using lamb wave methods, Smart Materials and Structures 11 (2) (2002) 269.

[9] X. Kong, J. Li, W. Collins, C. Bennett, S. Laflamme, H. Jo, A robust signal processing method for quantitative high-cycle fatigue crack monitoring using soft elastomeric capacitor sensors, in: SPIE Smart Structures and Materials and Nondestructive Evaluation and Health Monitoring, International Society for Optics and Photonics, 2017, pp. 101680B–101680B.

[10] X. Kong, J. Li, C. Bennett, W. Collins, S. Laflamme, Numerical simulation and experimental validation of a large-area capacitive strain sensor for fatigue crack monitoring, Measurement Science and Technology 27 (12) (2016) 124009.

[11] J. Tikka, R. Hedman, A. Silijander, Strain gauge capabilities in crack detection, in: 4th International Workshop on Structural Health Monitoring, 2003, pp. 15–17.

[12] T. Tallman, J. Hernandez, The effect of error and regularization norms on strain and damage identification via electrical impedance tomography in piezoresistive nanocomposites, NDT & E International 91 (2017) 156–163.

[13] T. Tallman, S. Gungor, G. Koo, C. Bakis, On the inverse determination of displacements, strains, and stresses in a carbon nanofiber/polyurethane nanocomposite from conductivity data obtained via electrical impedance tomography, Journal of Intelligent Material Systems and Structures (2017) 1–13.

[14] H. Dai, G. J. Gallo, T. Schumacher, E. T. Thostenson, A novel methodology for spatial damage detection and imaging using a distributed carbon nanotube-based composite sensor combined with electrical impedance tomography, Journal of Nondestructive Evaluation 35 (2) (2016) 1–15.

[15] M. Hallaji, A. Seppänen, M. Pour-Ghaz, Electrical impedance tomography-based sensing skin for quantitative imaging of damage in concrete, Smart Mater. Struct. 23 (8) (2014) 085001.

[16] T. Tallman, S. Gungor, K. Wang, C. Bakis, Damage detection and conductivity evolution in carbon nanofiber epoxy via electrical impedance tomography, Smart Mater. Struct. 23 (4) (2014) doi: 10.1088/0964–1726/23/4/045034.

[17] B. R. Loyola, V. La Saponara, K. J. Loh, T. M. Briggs, G. O'Bryan, J. L. Skinner, Spatial sensing using electrical impedance tomography, IEEE Sensors Journal 13 (6) (2013) 2357–2367.

[18] D. Smyl, R. Rashetnia, A. Seppänen, M. Pour-Ghaz, Can electrical resistance tomography be used for imaging unsaturated moisture flow in cement-based materials with discrete cracks?, Cement and Concrete Research 91 (2017) 61–72.

[19] D. Smyl, M. Hallaji, A. Seppänen, M. Pour-Ghaz, Quantitative electrical imaging of three-dimensional moisture flow in cement-based materials, International Journal of Heat and Mass Transfer 103 (2016) 1348–1358.

[20] D. Smyl, M. Hallaji, A. Seppänen, M. Pour-Ghaz, Three dimensional electrical imaging of moisture ingress in mortar, ACI Special Publication.

[21] M. Hallaji, A. Seppänen, M. Pour-Ghaz, Electrical resistance tomography to monitor unsaturated moisture flow in cementitious materials, Cement and Concrete Research 69 (2015) 10–18.

[22] A. Seppänen, M. Hallaji, M. Pour-Ghaz, A functionally layered sensing skin for the detection of corrosive elements and cracking, Structural Health Monitoring 16 (2) (2017) 215–224.

[23] M. Khadra, J.-F. Lataste, N. Burlion, T. Rougelot, J.-P. Carlier, Carbonation effect on measurements of electrical resistivity tomography, 2nd International Conference on Civil, Structural and Transportation Engineering.

[24] J. Mueller, S. Siltanen, Linear and Nonlinear Inverse Problems with Practical Applications, SIAM, 2012.

[25] J. Kaipio, E. Somersalo, Statistical and Computational Inverse Problems, Springer New York, 2005.

[26] M. Jehl, A. Dedner, T. Betcke, K. Aristovich, R. Klöfkorn, D. Holder, A fast parallel solver for the forward problem in electrical impedance tomography, IEEE Transactions on Biomedical Engineering 62 (1) (2015) 126–137.

[27] W. R. Lionheart, EIT reconstruction algorithms: pitfalls, challenges and recent developments, Physiological measurement 25 (1) (2004) 125.

[28] D. Isaacson, J. Mueller, J. Newell, S. Siltanen, Imaging cardiac activity by the d-bar method for electrical impedance tomography, Physiological Measurement 27 (5) (2006) S43.

[29] K. Knudsen, M. Lassas, J. L. Mueller, S. Siltanen, Regularized d-bar method for the inverse conductivity problem, Inverse Problems and Imaging 35 (4) (2009) 599.

[30] B. Gebauer, N. Hyvönen, Factorization method and irregular inclusions in electrical impedance tomography, Inverse Problems 23 (5) (2007) 2159.

[31] S. Schmitt, The factorization method for eit in the case of mixed inclusions, Inverse Problems 25 (6) (2009) 065012.

[32] A. Tamburrino, G. Rubinacci, M. Soleimani, W. Lionheart, A noniterative inversion method for electrical resistance, capacitance and inductance tomography for two phase materials, in: Proc. 3rd World Congress on Industrial Process Tomography, Canada, 2003, pp. 233–238.

[33] A. Tamburrino, G. Rubinacci, A new non-iterative inversion method for electrical resistance tomography, Inverse Problems 18 (6) (2002) 1809.

[34] H. Garde, S. Staboulis, Convergence and regularization for monotonicity-based shape reconstruction in electrical impedance tomography, Numerische Mathematik 135 (4) (2017) 1221–1251.

[35] A. Nissinen, L. Heikkinen, J. Kaipio, The bayesian approximation error approach for electrical impedance tomographyexperimental results, Measurement Science and Technology 19 (1) (2007) 015501.

[36] A. Lipponen, A. Seppanen, J. P. Kaipio, Electrical impedance tomography imaging with reduced-order model based on proper orthogonal decomposition, Journal of Electronic Imaging 22 (2) (2013) 023008.

[37] M. Hallaji, M. Pour-Ghaz, A new sensing skin for qualitative damage detection in concrete elements: Rapid difference imaging with electrical resistance tomography, NDT & E International 68 (2014) 13–21.

[38] M. Hallaji, A. Seppänen, M. Pour-Ghaz, Electrical impedance tomography-based sensing skin for quantitative imaging of damage in concrete, Smart Materials and Structures 23 (8) (2014) 1–13.

[39] F. Vecchio, Disturbed stress field model for reinforced concrete: formulation, Journal of structural engineering 126 (9) (2000) 1070–1077.

[40] D. Liu, V. Kolehmainen, S. Siltanen, A. Laukkanen, A. Seppänen, Estimation of conductivity changes in a region of interest with electrical impedance tomography, Inverse Probl. Imag. 9(1) (2015) 211–229.

[41] D. Liu, V. Kolehmainen, S. Siltanen, A. Seppänen, A nonlinear approach to difference imaging in EIT; assessment of the robustness in the presence of modelling errors, Inverse Problems 31 (3) (2015) 035012.

[42] D. S. Holder, Electrical impedance tomography: methods, history and applications, CRC Press, 2004.

[43] D. J. LaBrecque, X. Yang, Difference inversion of ERT data: A fast inversion method for 3-d in situ monitoring, Journal of Environmental & Engineering Geophysics 6 (2) (2001) 83–89.

[44] C. R. Miller, P. S. Routh, T. R. Brosten, J. P. McNamara, Application of time-lapse ert imaging to watershed characterization, Geophysics 73 (3) (2008) G7–G17.

[45] K.-S. Cheng, D. Isaacson, J. Newell, D. Gisser, Electrode models for electric current computed tomography, IEEE T. Bio-Med. Eng. 36 (9) (1989) 918–924.

[46] E. Somersalo, M. Cheney, D. Isaacson, Existence and uniqueness for electrode models for electric current computed tomography, SIAM Jour. on Appl. Math. 52 (4) (1992) 1023–1040.

[47] P. J. Vauhkonen, M. Vauhkonen, T. Savolainen, J. P. Kaipio, Three-dimensional electrical impedance tomography based on the complete electrode model, IEEE T. Biomedical Eng. 46(9) (1999) 1150–1160.

[48] M. Vauhkonen, W. Lionheart, L. Heikkinen, P. Vauhkonen, J. Kaipio, A MATLAB package for the EIDORS project to reconstruct two-dimensional EIT images, Physiol. Meas. 22 (2001) 107–111.

[49] A. Seppänen, M. Hallaji, M. Pour-Ghaz, Electrical impedance tomography-based sensing skin for detection of damage in concrete, in: Proceedings of the 11th European Conference on Non-Destructive Testing (ECNDT 2014), Prague, Czech Republic, 2014, pp. 6–10.

[50] A. Fiacco, G. McCormick, Nonlinear Programming: Sequential Unconstrained Minimization Techniques, no. 4, Siam, 1990.

[51] G. González, V. Kolehmainen, A. Seppänen, Isotropic and anisotropic total variation regularization in electrical impedance tomography, Computers & Mathematics with Applications 74 (3) (2017) 564–576.

[52] P. Vauhkonen, M. Vauhkonen, T. Savolainen, J. Kaipio, Three-dimensional electrical impedance tomography based on the complete electrode model, IEEE T. Biomedical Eng. 46 (9) (1999) 1150–1160.

[53] P. Wong, F. Vecchio, Vector2 and formworks users manual, Civil Engineering, University of Toronto, Toronto, Ont.

[54] I. Chak, Janus: A post-processor for vector analysis software, Ph.D. thesis (2013).

[55] ACI committee and American Concrete Institute and international organization for standardization: Building code requirements for structural concrete (ACI 318-08) and commentary, American Concrete Institute, 2008.

[56] E. Syroka-Korol, J. Tejchman, Experimental investigations of size effect in reinforced concrete beams failing by shear, Engineering Structures 58 (2014) 63–78.